International Journal of Engineering Inventions
e-ISSN: 2278-7461, p-ISSN: 2319-6491
Volume 15, Issue 7 [July 2026] PP: 13-29

Scaling-Factor-Tuned NARMA-L2 Neural Control for Robust Frequency Regulation of a Hydropower-Photovoltaic System: Comparative Evaluation against PI and PID

Nguyen Huu Thang
Thanh Hoa College of Industry, Thanhhoa, Vietnam
Corresponding Author: thangnh.25TS0000011@epu.edu.vn

ABSTRACT: *This paper develops a scaling-factor-tuned nonlinear autoregressive moving-average L2 (SF-NARMA-L2) neural controller for frequency regulation of a hydropower plant exposed to distributed photovoltaic (PV) variability. The benchmark retains permanent and transient droop, governor-servomotor dynamics, the hydraulic-turbine non-minimum-phase response, generator-load inertia, frequency-sensitive demand, PV power lag, guide-vane saturation, and gate-rate limitation. A multi-input NARMA-L2 model is identified from deterministic excitation data generated over a ±25% family of plant parameters. Its input-affine nonlinear functions are approximated by a shallow extreme-learning network, while a damped inverse provides the supplementary command. The output scaling factor is selected by a multi-scenario objective rather than assigned heuristically. SF-NARMA-L2 is compared with fixed PI and PID controllers under simultaneous step load/PV changes, a cloud-passage ramp, band-limited random solar-load fluctuations, and a severe disturbance applied to a perturbed plant. The selected factor, α* = 2.75, reduces the frequency integral absolute error relative to PID by 42.6%, 44.3%, 41.5%, and 39.1% in the four cases, respectively. Peak frequency deviations decrease by 15.8-23.6%. Across twenty Monte Carlo plants, the mean IAE reductions are 44.1% under random forcing and 41.7% in the severe uncertain case. All locally linearized sampled-data models are Schur stable, and positive-definite solutions of the discrete Lyapunov equation are obtained. The improvement requires greater command variation, particularly under random forcing, although all imposed actuator limits remain satisfied. These results demonstrate that scaling-factor tuning materially strengthens NARMA-L2 disturbance rejection and parameter robustness, while PI and PID retain advantages in implementation simplicity and actuator moderation.*

Keywords: *hydropower; photovoltaic generation; frequency regulation; NARMA-L2; neural control; scaling factor; Lyapunov stability; parameter uncertainty.*

NOMENCLATURE

Symbol	Description	Unit
D	Frequency-sensitive load coefficient	pu/Hz
F, G	Input-affine NARMA-L2 nonlinear functions	-
g	Incremental guide-vane position	pu
H	Equivalent inertia constant	s
R, R_t	Permanent and transient droop	Hz/pu
T_g, T_w, T_r	Governor, water-starting, and reset constants	s
T_{PV}	Aggregate PV active-power time constant	s
u	Supplementary speed-changer command	pu
Δf	Generator-frequency deviation	Hz
$\Delta P_L, \Delta P_{PV}$	Load and PV active-power deviations	pu
α	NARMA-L2 output scaling factor	-
$\rho(A_{cl})$	Closed-loop spectral radius	-

Date of Submission: 06-07-2026 Date of acceptance: 17-07-2026

I. INTRODUCTION

The present study aims to experimentally investigate the solar water distillation characteristics of spherical dome as a dehumidifier surface. Parameters that can be used to measure the performance of this type of solar water distillation are also presented, investigated and estimated. The effects of some geometric parameters of the spherical dome on the performance of the solar water distillation will be investigated. The experiments have been carried out to provide comprehensive study of the solar water distillation by using spherical dome as a dehumidifier surface at different key design parameter.

Hydropower remains a valuable provider of inertia, primary reserve, and flexible generation. Its governor dynamics, however, differ fundamentally from those of a thermal unit. Water-column inertia creates an initial inverse mechanical-power response, and the interaction among transient droop, gate motion, conduit dynamics, and generator inertia can produce a lightly damped frequency transient [1]-[7]. Variable-speed hydropower can increase operational flexibility, yet it also requires coordinated modeling and control of hydraulic and electromechanical dynamics [2], [3].

Distributed PV changes the regulation problem. PV active power reduces net demand during normal operation, but irradiance ramps and cloud passages can create fast power imbalances without adding synchronous inertia. Modern frequency-control studies therefore consider renewable uncertainty, hybrid resources, storage, and converter-dominated dynamics [8]-[14]. These studies consistently show that a controller tuned only at one operating point may lose performance when renewable power and plant parameters vary simultaneously.

PI and PID controllers remain common because they are transparent, inexpensive, and straightforward to commission. Advanced designs based on linear matrix inequalities, fuzzy logic, sliding-mode control, optimization, and reinforcement learning can improve disturbance rejection [15]-[23], [29]-[36]. Their benefits are nevertheless accompanied by additional tuning, sensing, or computational requirements. Neural input-output linearization offers another route. NARMA-L2 control approximates the nonlinear plant by an input-affine predictor and computes an inverse command online [24]-[26]. Extreme-learning formulations reduce training cost by solving the output weights in one regularized least-squares step [27], [28].

A practical weakness remains. The raw inverse gain is sensitive to normalization, prediction horizon, model error, and the small estimated input gain of the slow hydro plant. An arbitrary scaling factor may underuse the learned inverse or generate excessive command reversals. Moreover, favorable nominal plots alone do not establish robustness. Parameter uncertainty, actuator constraints, random PV-load forcing, and a stability statement must be addressed together.

This study makes four contributions. First, it formulates a reproducible nonlinear hydropower-PV benchmark that retains the principal hydraulic inverse response and physical gate constraints. Second, it proposes an SF-NARMA-L2 controller whose output scaling factor is selected by a multi-scenario validation criterion. Third, it compares the proposed method with PI and PID using identical constraints under four deterministic cases and twenty uncertain Monte Carlo plants. Fourth, it provides a local discrete-time Lyapunov analysis and interprets the effect of bounded neural residuals and renewable disturbances.

II. SPEED AND FREQUENCY REGULATION OF THE HYDRO-PV PLANT

A. Regulation structure

The governor combines permanent droop with a supplementary command. Droop provides decentralized primary sharing, whereas the supplementary loop restores frequency after the transient. Transient-droop compensation is retained because the hydraulic turbine initially responds in the direction opposite to a rapid gate movement [1], [4]. The distributed PV source is connected at the generator-load bus. Therefore, the incremental net disturbance is

$$\Delta P_d(t) = \Delta P_L(t) - \Delta P_{PV}(t). \tag{1}$$

A positive load increment and a PV reduction act in the same direction. PI and PID use frequency feedback only. SF-NARMA-L2 additionally uses measured or estimated load and PV deviations in its regressor. Figure 1 shows the common plant and signal structure.

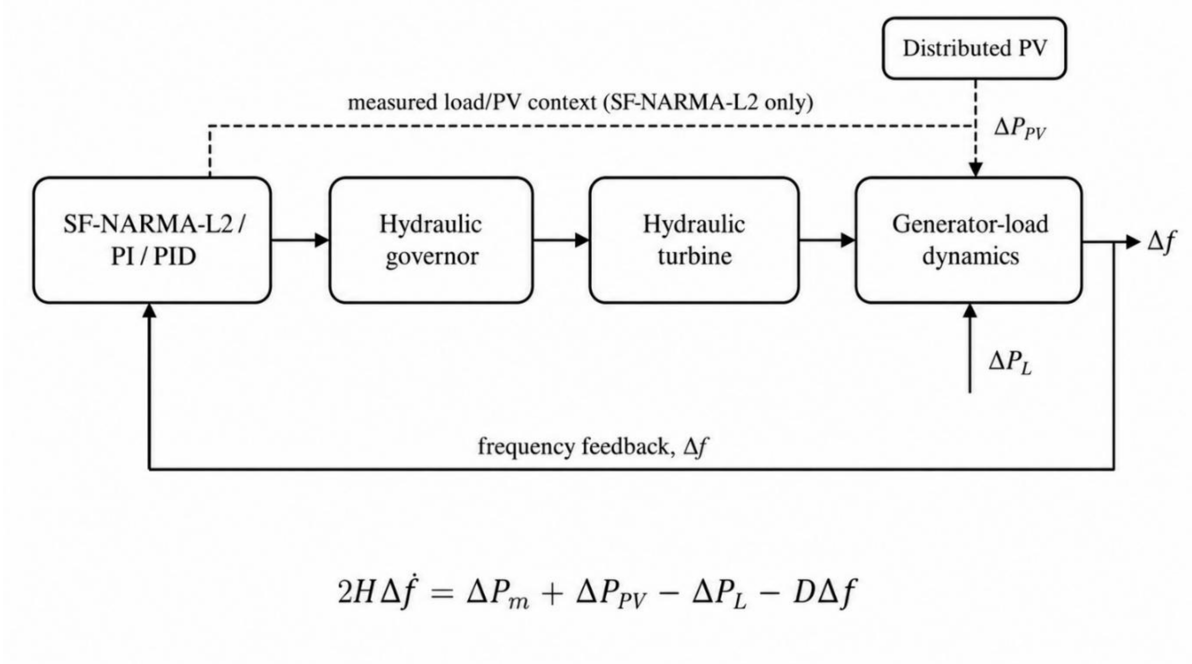

Fig. 1. Hydropower plant with distributed PV generation and the common closed-loop signal structure

B. Control objectives

The design must balance several objectives. The peak, root-mean-square (RMS), and accumulated frequency deviations should be small. Constant imbalances must be rejected without steady-state error. Gate-position and gate-rate limits must be respected. Performance should also remain acceptable when inertia, damping, droop, time constants, and PV dynamics vary together. Because intermittent PV can demand continuous corrective action, command RMS and total variation are reported beside the frequency indices. This reveals the actuator cost of improved regulation.

III. MATHEMATICAL MODEL

A. Governor and transient-droop compensator

Let u be the supplementary speed-changer command and v the signal after permanent droop:

$$v(t) = u(t) - \frac{\Delta f(t)}{R}. \tag{2}$$

The transient-droop compensator is represented by

$$G_r(s) = \frac{1 + T_r s}{1 + aT_r s}, \qquad a = \frac{R_t}{R}. \tag{3}$$

With internal state z, its time-domain realization is

$$\dot{z}(t) = \frac{-z(t) + v(t)}{aT_r}. \tag{4}$$

$$w(t) = \frac{v(t)}{a} + \left(1 - \frac{1}{a}\right) z(t). \tag{5}$$

The guide-vane servomotor includes both rate and magnitude constraints:

$$\dot{g}(t) = \mathrm{sat}_{-\dot{g}_{max}}^{\dot{g}_{max}}\left(\frac{-g(t) + w(t)}{T_g}\right). \tag{6}$$

$$|g(t)| \le g_{max}. \tag{7}$$

The constraints are enforced inside each numerical integration step and are identical for all controllers.

B. Hydraulic turbine

The non-elastic water-column model is

$$G_t(s) = \frac{\Delta P_m(s)}{g(s)} = \frac{1 - T_w s}{1 + 0.5T_w s}. \tag{8}$$

A state realization that preserves the steady-state gain and right-half-plane zero is

$$\dot{q}(t) = \frac{-q(t) + g(t)}{0.5T_w}. \tag{9}$$

$$\Delta P_m(t) = 3q(t) - 2g(t). \tag{10}$$

The direct term $-2g$ produces the initial inverse response. Consequently, an aggressive command may deepen the first frequency excursion even when the final response is faster.

C. PV source and generator-load balance

The aggregate PV active-power response is modeled as

$$T_{PV}\Delta\dot{P}_{PV}(t) = -\Delta P_{PV}(t) + \Delta P_{PV}^{\star}(t). \tag{11}$$

The generator-load balance is

$$2H\Delta\dot{f}(t) = \Delta P_m(t) + \Delta P_{PV}(t) - \Delta P_L(t) - D\Delta f(t). \tag{12}$$

The state vector is

$$\mathbf{x}(t) = [\Delta f(t) \quad z(t) \quad g(t) \quad q(t) \quad \Delta P_{PV}(t)]^T. \tag{13}$$

Parameter uncertainty is introduced as

$$p_i = p_{i0}(1 + \delta_i), \qquad |\delta_i| \le 0.25. \tag{14}$$

The nonlinear system is integrated using fourth-order Runge-Kutta with $T_s = 0.1$ s. Table 1 lists the nominal values.

Table 1. Nominal hydropower-PV model and actuator parameters

Parameter	Value	Parameter	Value
H	5.00 s	D	1.00 pu/Hz
R	0.05 Hz/pu	R_t	0.30 Hz/pu
T_g	0.20 s	T_w	1.00 s
T_r	5.00 s	T_{PV}	0.35 s
g_{max}	0.35 pu	$\dot{g}_{max}$	0.15 pu/s
u_{max}	0.12 pu	command increment limit	0.025 pu/sample
Sampling period	0.10 s	uncertainty range	±25%

IV. CONTROL METHODOLOGIES

A. PI and PID benchmarks

The regulation error is $e(k) = -\Delta f(k)$. The PI controller is

$$\xi(k) = \xi(k-1) + T_s e(k). \tag{15}$$

$$u_{PI}(k) = K_p e(k) + K_i \xi(k). \tag{16}$$

For PID, a filtered difference is used:

$$D_f(k) = 0.9D_f(k-1) + 0.1\frac{e(k) - e(k-1)}{T_s}. \tag{17}$$

$$u_{PID}(k) = K_p e(k) + K_i \xi(k) + K_d D_f(k). \tag{18}$$

The selected gains are $[K_p, K_i] = [2.0, 0.6]$ for PI and $[K_p, K_i, K_d] = [2.5, 0.8, 0.3]$ for PID. Saturation and integral back-calculation are applied in both cases. The gains are fixed before the final uncertainty tests.

B. Input-affine NARMA-L2 model

For prediction delay d, the nonlinear sampled-data input-output model is approximated by

$$\Delta f(k+d) = F\big(\mathbf{z}(k)\big) + G\big(\mathbf{z}(k)\big)u(k) + \varepsilon_N(k). \tag{19}$$

The augmented regressor is

$$\mathbf{z}(k) = [\mathbf{x}^T(k) \quad \Delta P_L(k) \quad \Delta P_{PV}^{\star}(k) \quad u(k-1)]^T. \tag{20}$$

Training data are generated from eight deterministic excitation experiments. In each experiment, H, D, R, R_t, T_g, T_w, T_r, and T_{PV} are independently varied within ±25%. A shallow network with 200 hyperbolic-tangent hidden nodes maps the regressor to the affine terms $[F, G]$. The output weights follow ridge-regularized extreme learning [27], [28]:

$$\mathbf{B} = (\mathbf{H}^T\mathbf{H} + \lambda\mathbf{I})^{-1}\mathbf{H}^T\mathbf{Y}, \qquad \lambda = 10^{-4}. \tag{21}$$

The held-out regression for F achieves $R^2 = 0.991$ (Fig. 4). This value is reported as an identification diagnostic, not as a substitute for closed-loop validation.

C. Damped inverse and scaling-factor tuning

The regularized inverse command is

$$u_{inv}(k) = \frac{\hat{G}(k)}{\hat{G}^2(k) + \rho}\big[-\hat{F}(k)\big], \qquad \rho = 0.002. \tag{22}$$

A leaky integrator eliminates persistent bias:

$$\xi_N(k) = (1 - \ell T_s)\xi_N(k-1) - T_s\Delta f(k), \qquad \ell = 0.03\ \mathrm{s}^{-1}. \tag{23}$$

The proposed scaled and smoothed command is

$$u_t(k) = \mathrm{sat}[\alpha u_{inv}(k) + K_{IN}\xi_N(k)], \qquad K_{IN} = 0.03. \tag{24}$$

$$u(k) = (1-\beta)u(k-1) + \beta u_t(k), \qquad \beta = 0.65. \tag{25}$$

An equilibrium offset is removed from $\hat{F}$ so that the nominal origin produces zero supplementary command. The scaling factor is selected from $\alpha \in \{0.50, 0.75, \dots, 3.00\}$ by minimizing

$$J_{val} = \sum_{s \in \mathcal{S}_{val}} \big(3\, IAE_s + 30\, f_{pk,s} + 3\, u_{rms,s} + 0.03\, TV_{u,s}\big). \tag{26}$$

The validation set contains the step-PV, cloud-ramp, and random cases. The minimum is $J_{val} = 3.1794$ at $\alpha^{\star} = 2.75$. Figure 2 summarizes the complete offline-online procedure, while Fig. 3 shows that the objective is shallow near its minimum. This observation is useful: the selected factor is effective, but the method is not critically dependent on a single numerical grid point.

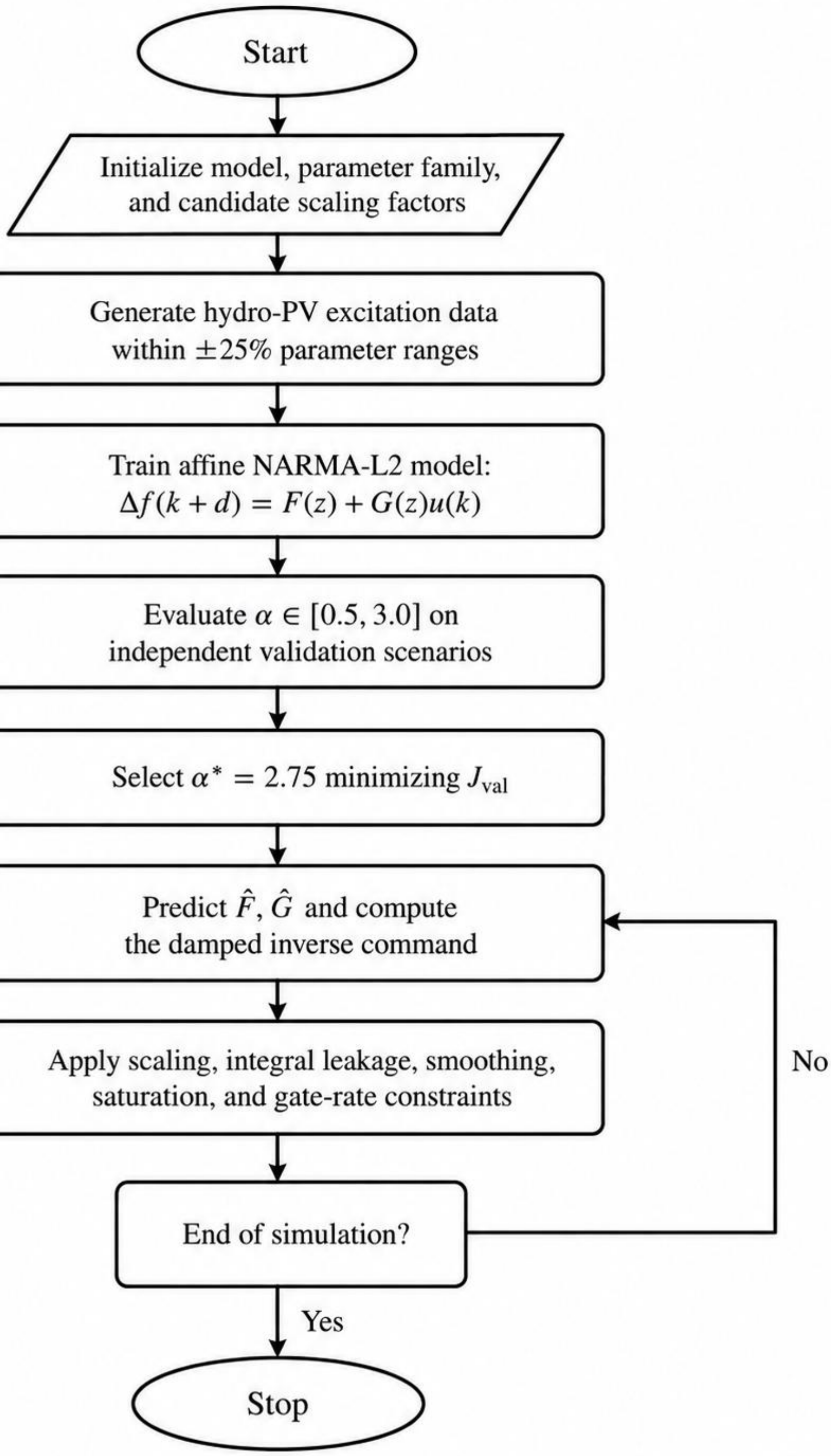

Fig. 2. Offline identification, scaling-factor selection, and online SF-NARMA-L2 implementation

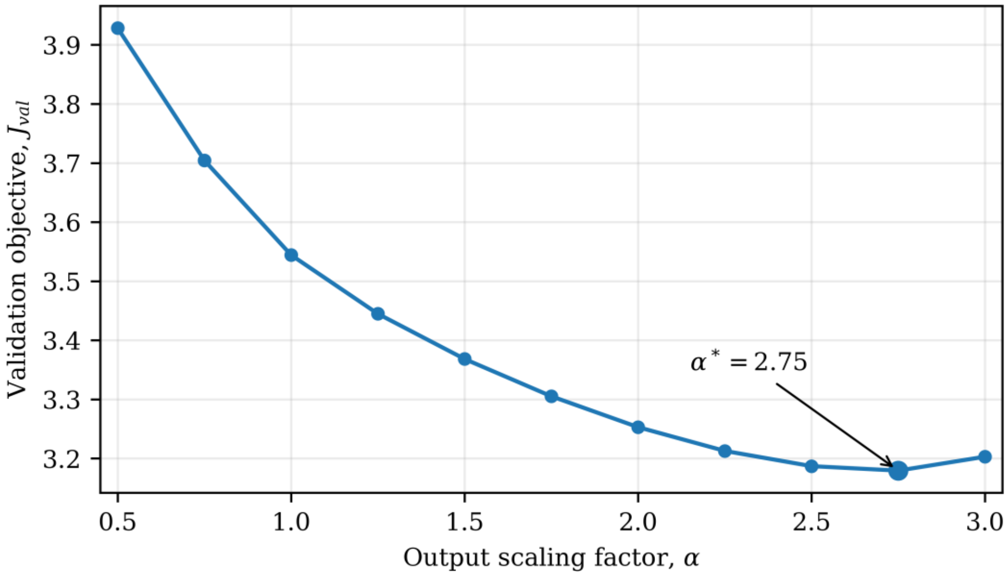

Fig. 3. Multi-scenario tuning of the NARMA-L2 output scaling factor

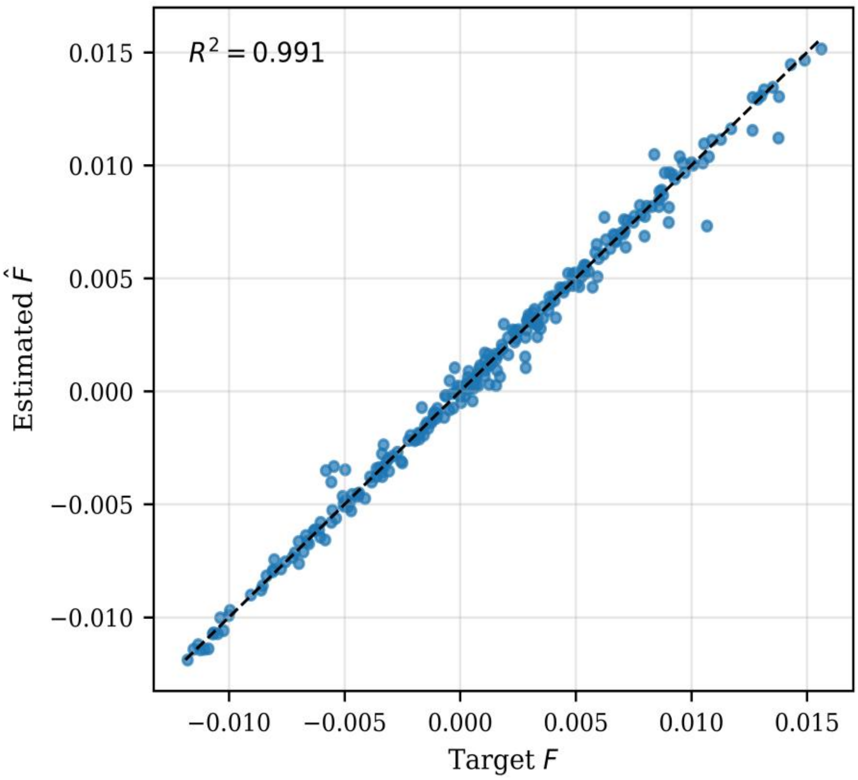

Fig. 4. Held-out regression of the estimated NARMA-L2 affine term F

C. Lyapunov stability analysis

The implemented controllers include saturation, rate limitation, and a bounded neural residual. A global quadratic proof would therefore be stronger than the model supports. Stability is established locally around the zero-disturbance equilibrium, where the limits are inactive, and practical stability is then stated for bounded exogenous inputs.

Let $\boldsymbol{\chi}$ contain the plant states and the relevant controller-memory states. The locally linearized sampled-data model is

$$\boldsymbol{\chi}(k+1) = A_{cl}\boldsymbol{\chi}(k) + B_w w(k). \tag{27}$$

For $w(k) = 0$, consider

$$V(k) = \boldsymbol{\chi}^T(k) P \boldsymbol{\chi}(k), \qquad P = P^T > 0. \tag{28}$$

The discrete Lyapunov equation is

$$A_{cl}^T P A_{cl} - P = -Q, \qquad Q = I. \tag{29}$$

When $\rho(A_{cl}) < 1$, the solution P is positive definite and

$$\Delta V(k) = -\boldsymbol{\chi}^T(k) Q \boldsymbol{\chi}(k) < 0. \tag{30}$$

For bounded $w(k)$, the cross terms can be bounded using Young's inequality, which yields

$$\Delta V(k) \leq -c_1 \parallel \boldsymbol{\chi}(k) \parallel^2 + c_2 \parallel w(k) \parallel^2. \tag{31}$$

Thus, the origin is locally asymptotically stable in the unforced case and locally input-to-state practically stable for bounded PV/load disturbances and identification residuals. This conclusion is deliberately local; global stability under persistent saturation is not claimed.

VI. SIMULATION DESIGN AND REPRODUCIBILITY

All controllers use the same plant model, sampling period, command saturation, gate saturation, and gate-rate limit. Four principal cases are investigated: (1) simultaneous step load and abrupt PV changes; (2) a cloud-passage PV ramp with repeated load changes; (3) band-limited random load and PV fluctuations; and (4) a severe combined disturbance applied to a plant whose principal parameters are perturbed within ±25%. Twenty additional parameter realizations are simulated for the random and severe cases.

The principal indices are

$$IAE = \int_0^T |\Delta f(t)| \, dt. \tag{32}$$

$$ITAE = \int_0^T t \, |\Delta f(t)| \, dt. \tag{33}$$

$$f_{RMS} = \sqrt{\frac{1}{T}\int_0^T \Delta f^2(t) \, dt}. \tag{34}$$

$$u_{RMS} = \sqrt{\frac{1}{T}\int_0^T u^2(t) \, dt}. \tag{35}$$

$$TV_u = \sum_{k=1}^{N-1} |u(k+1) - u(k)|. \tag{36}$$

Frequency quality is assessed first. Command RMS, command total variation, and peak guide-vane position are then used to quantify actuator burden.

To execute the simulation process, the main settings are $T_s = 0.1$ s, $T = 160$ s, prediction delay $d = 30$ samples, 200 hidden nodes, ridge coefficient 10^{-4}, eight identification experiments, and twenty Monte Carlo plants.

V. RESULTS AND DISCUSSION

A. Scaling-factor and identification results

The validation curve in Fig. 3 decreases rapidly between $\alpha = 0.5$ and approximately 2.0. It then flattens and reaches its minimum at $\alpha^\star = 2.75$. Low factors do not sufficiently compensate the slow water-column response. Beyond the minimum, the frequency benefit becomes marginal while command reversals increase. The regression plot in Fig. 4 is concentrated around the 45° line and gives $R^2 = 0.991$. More importantly, the subsequent closed-loop cases remain stable and accurate when the physical parameters differ from those used in any single training experiment.

B. Step load and abrupt PV changes

Figure 5 contains simultaneous changes in load and PV power. The first event exposes the hydraulic inverse response. SF-NARMA-L2 generates a stronger but rate-limited counter-command and recovers more quickly than PI and PID. Its peak frequency deviation is 10.631 mHz, compared with 13.915 mHz for PID. The IAE falls from 0.2271 to 0.1305 Hz·s, a 42.6% reduction. The neural controller also decreases RMS frequency error by 36.4%. These gains are not free: command total variation rises from 0.226 to 1.250 pu. Peak gate movement nevertheless remains slightly lower than for PID, which confirms that the additional activity consists mainly of small reversals rather than a larger absolute opening.

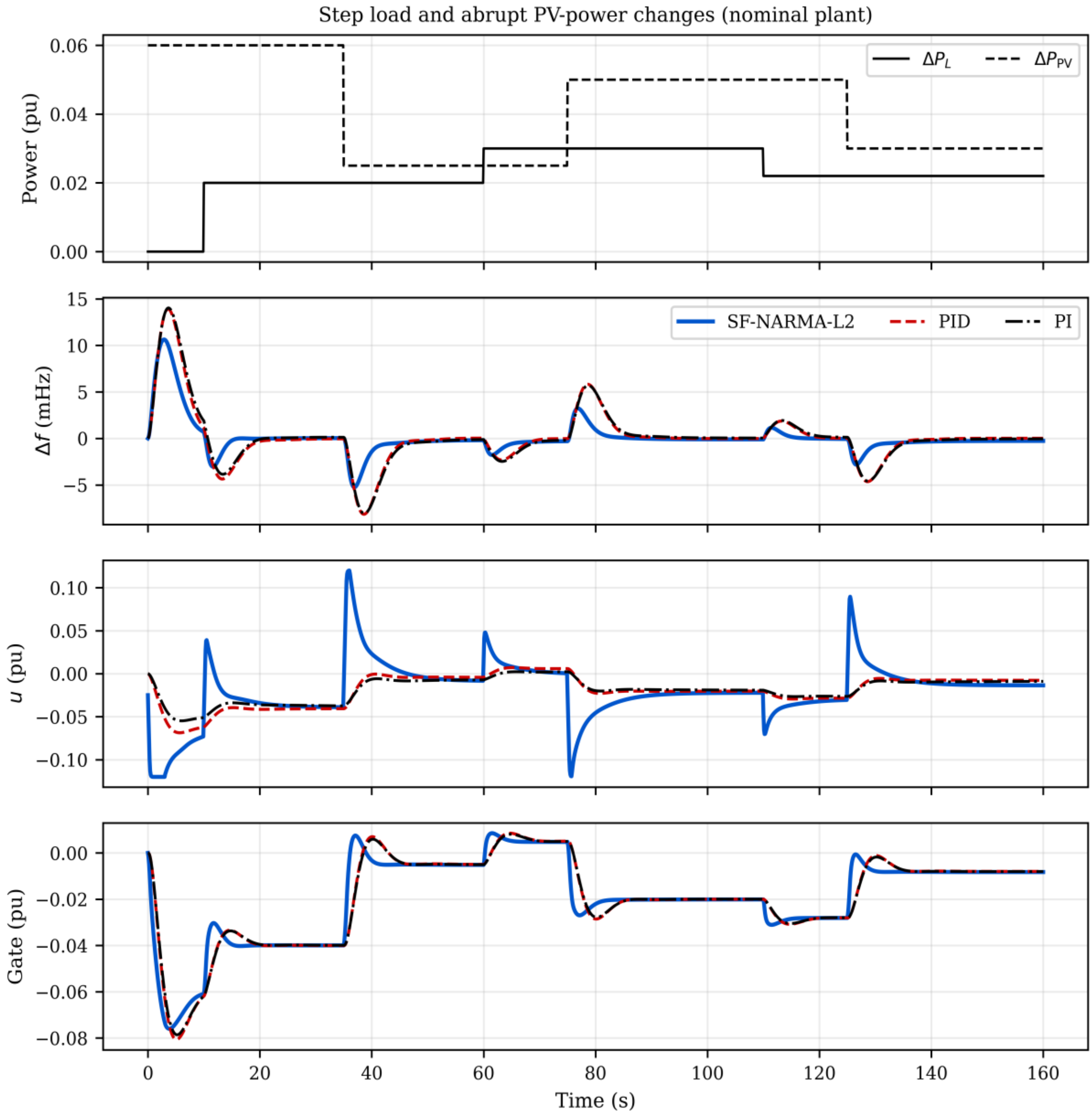

Fig. 5. Responses to simultaneous step load and abrupt PV-power changes

C. Cloud-passage PV ramp

The cloud-ramp case in Fig. 6 is slower than an abrupt PV trip but persists for a longer interval. The classical integral loops remove the final bias; however, they follow the extended imbalance with larger frequency displacement. SF-NARMA-L2 anticipates the finite-horizon effect through the learned regressor. Peak and RMS deviations are reduced by 20.8% and 33.0% relative to PID. IAE decreases by 44.3%, and ITAE decreases by

51.5%. The ITAE result is particularly relevant because it shows that the proposed method suppresses long-duration deviations rather than only clipping the first peak.

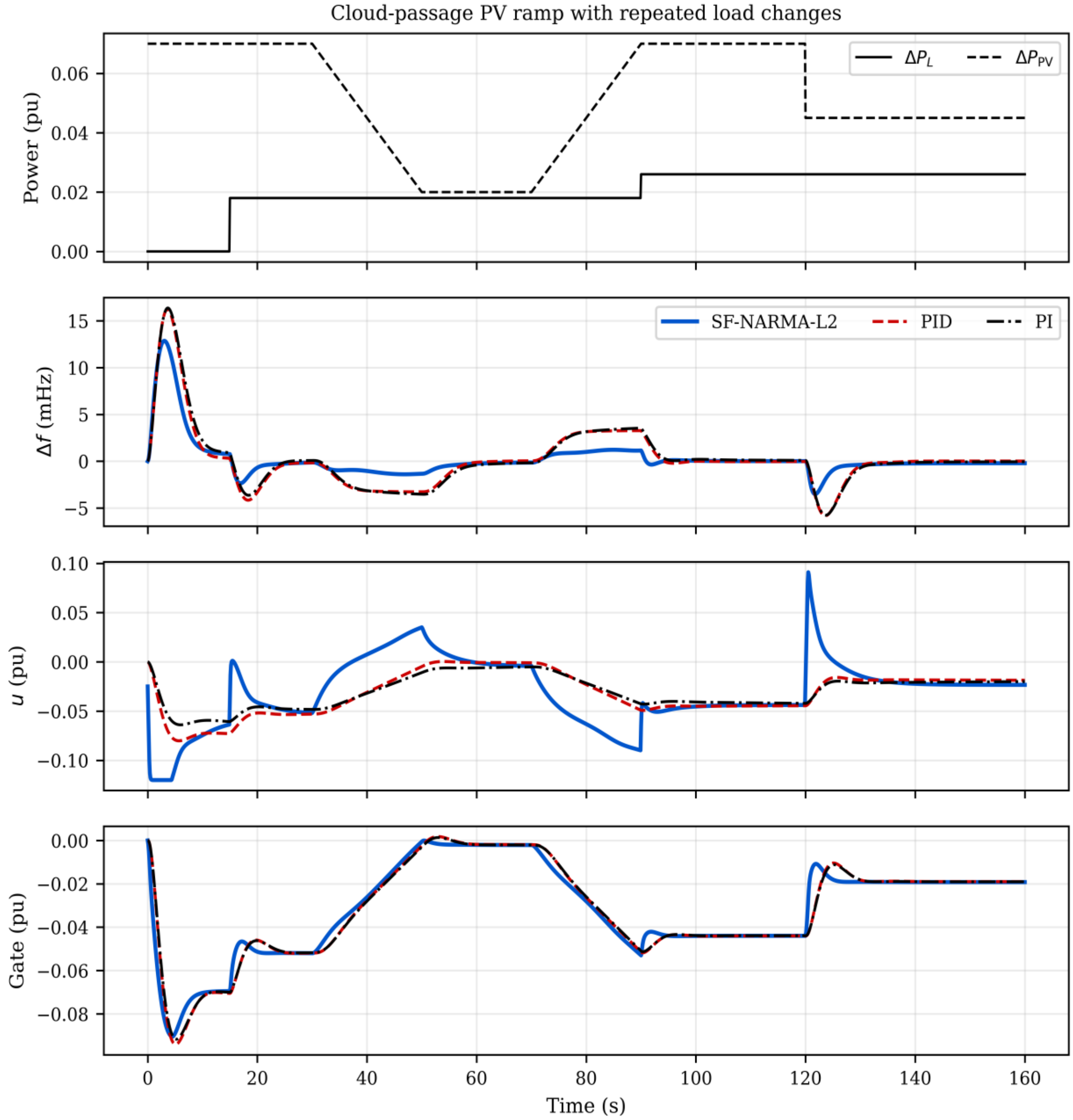

Fig. 6. Responses to a cloud-passage PV ramp with repeated load changes

D. Random solar-load fluctuations

Figure 7 is the most demanding actuator test. The random input is band limited, but it repeatedly changes direction. SF-NARMA-L2 keeps the frequency trace closest to zero: RMS error decreases from 3.976 to 2.416 mHz, and IAE decreases from 0.5182 to 0.3032 Hz·s. The benefit is accompanied by a pronounced increase in command variation, from 0.869 to 7.384 pu. This trade-off should not be hidden. It indicates that a fatigue-aware penalty or adaptive scaling law would be valuable when guide-vane wear is a dominant operational objective. Even in this case, the gate-position and gate-rate constraints are not violated.

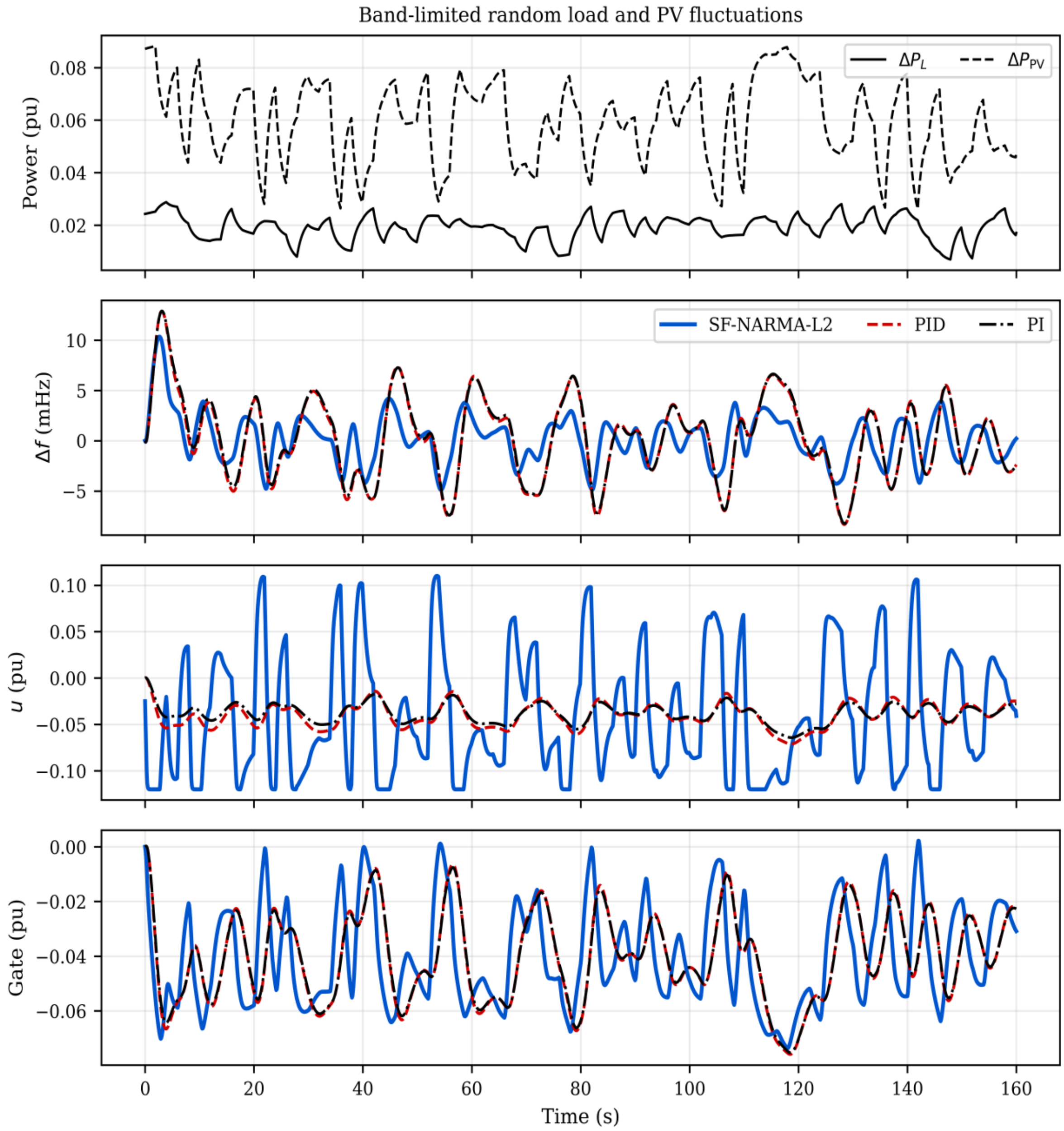

Fig. 7. Responses to band-limited random load and PV fluctuations

E. Severe disturbance with parameter uncertainty

The severe case combines large power changes with a perturbed plant. Figure 8 shows that all controllers remain stable, but PI and PID exhibit deeper excursions and slower recovery. SF-NARMA-L2 lowers peak deviation by 15.8%, RMS error by 29.6%, IAE by 39.1%, and ITAE by 45.3% relative to PID. The smaller percentage improvement in the first peak is physically plausible: rate limitation and the turbine's right-half-plane zero restrict how rapidly any controller can reverse the initial water-column response. The larger IAE and ITAE improvements demonstrate that the learned controller is most effective after the unavoidable first transient.

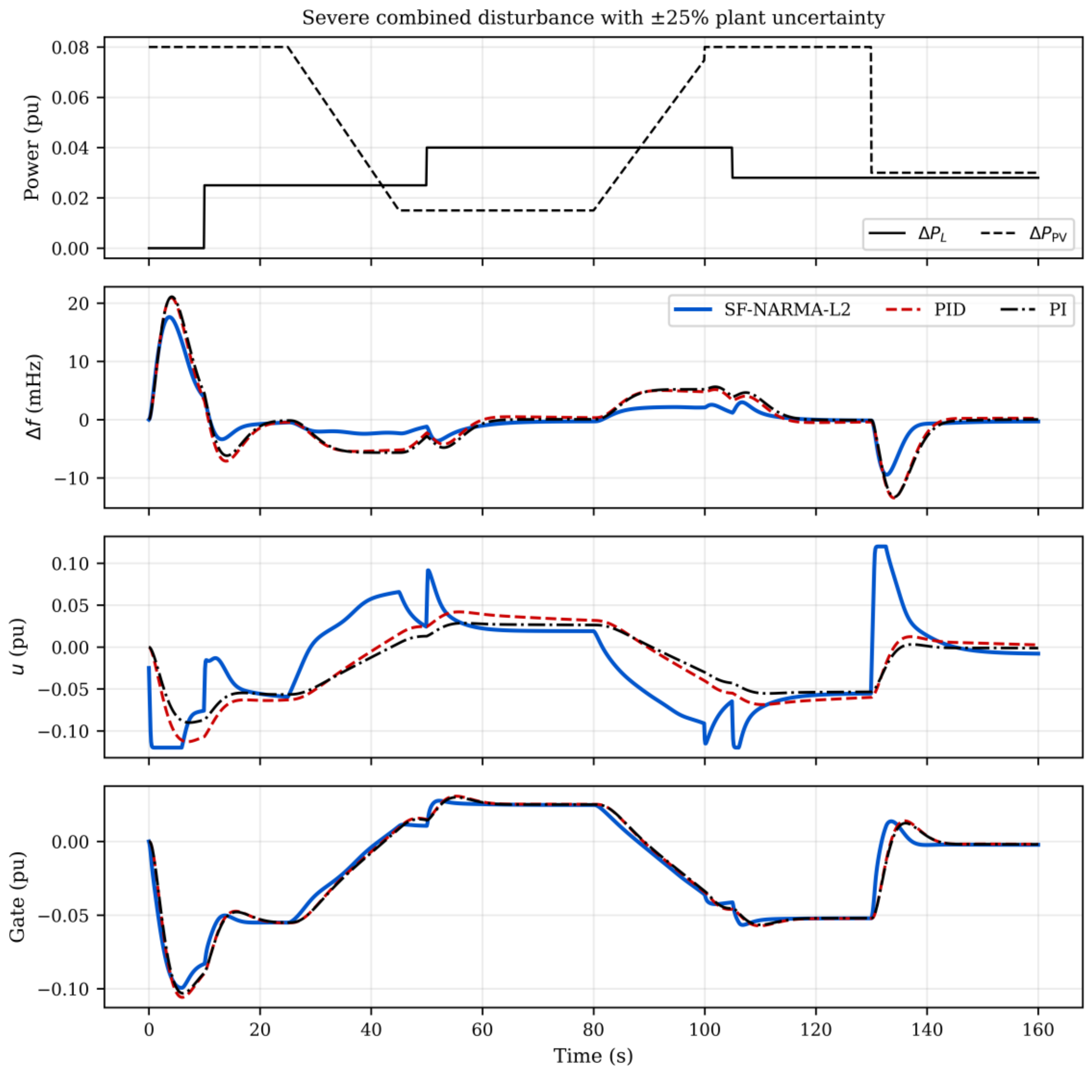

Fig. 8. Severe combined disturbance with simultaneous ±25% plant-parameter uncertainty

F. Quantitative comparison

Table 2. Main-scenario performance and actuator indices

Scenario	Controller	Peak (mHz)	RMS (mHz)	IAE (Hz·s)	ITAE (Hz·s²)	RMS u (pu)	TV u (pu)	Peak $\lvert g \rvert$ (pu)
Step load and abrupt PV change	SF-NARMA-L2	10.631	1.848	0.1305	5.924	0.0384	1.250	0.0760
	PI	14.027	2.950	0.2399	11.610	0.0229	0.179	0.0786
	PID	13.915	2.906	0.2271	10.546	0.0261	0.226	0.0806
Cloud-passage PV ramp	SF-NARMA-L2	12.855	2.111	0.1503	6.180	0.0456	0.793	0.0906
	PI	16.365	3.231	0.2858	13.911	0.0343	0.199	0.0917
	PID	16.234	3.152	0.2698	12.746	0.0381	0.252	0.0941
Random solar-load fluctuation	SF-NARMA-L2	10.343	2.416	0.3032	22.193	0.0770	7.384	0.0737
	PI	12.896	3.959	0.5151	37.857	0.0395	0.660	0.0753
	PID	12.879	3.976	0.5182	38.351	0.0422	0.869	0.0759

Scenario	Controller	Peak (mHz)	RMS (mHz)	IAE (Hz·s)	ITAE (Hz·s²)	RMS u (pu)	TV u (pu)	Peak $\|g\|$ (pu)
Severe disturbance with ±25% uncertainty	SF-NARMA-L2	17.604	3.571	0.3203	17.498	0.0561	1.163	0.0994
	PI	21.096	5.199	0.5312	32.350	0.0390	0.359	0.1031
	PID	20.919	5.073	0.5260	32.007	0.0472	0.471	0.1058

Table 2 confirms a consistent frequency-performance ranking. SF-NARMA-L2 is best in peak, RMS, IAE, and ITAE for every case. PI and PID are close to one another, with PID generally providing a modest transient improvement. The proposed controller also produces the smallest peak gate position in all four cases. By contrast, its command RMS and total variation are larger. Table 3 makes that trade-off explicit.

Table 3. SF-NARMA-L2 change relative to PID. Positive frequency entries denote reductions; positive actuator entries denote increases

Scenario	Peak reduction (%)	RMS reduction (%)	IAE reduction (%)	ITAE reduction (%)	RMS u change (%)	TV u change (%)
Step load and abrupt PV change	23.6	36.4	42.6	43.8	+47.3	+453.2
Cloud-passage PV ramp	20.8	33.0	44.3	51.5	+19.7	+214.7
Random solar-load fluctuation	19.7	39.2	41.5	42.1	+82.3	+750.0
Severe disturbance with ±25% uncertainty	15.8	29.6	39.1	45.3	+18.7	+147.0

The IAE reduction remains within a narrow 39.1-44.3% range despite the different disturbance spectra. This consistency is stronger evidence than improvement in one nominal step response. Command total variation is the principal cost, especially in the random case. Therefore, the proposed method is most attractive when frequency quality and renewable disturbance rejection dominate, whereas PID remains credible when actuator conservatism and commissioning simplicity are primary.

G. Monte Carlo robustness

Figure 9 and Table 4 summarize twenty uncertain plants for both random and severe forcing. Under random forcing, SF-NARMA-L2 reduces mean IAE by 44.1%, mean peak deviation by 35.0%, and mean RMS frequency error by 43.2% relative to PID. Under severe forcing, the corresponding reductions are 41.7%, 17.1%, and 30.5%. The worst-case IAE also remains below those of the classical controllers. The distributions are compact, showing that the improvement is not produced by a few favorable realizations.

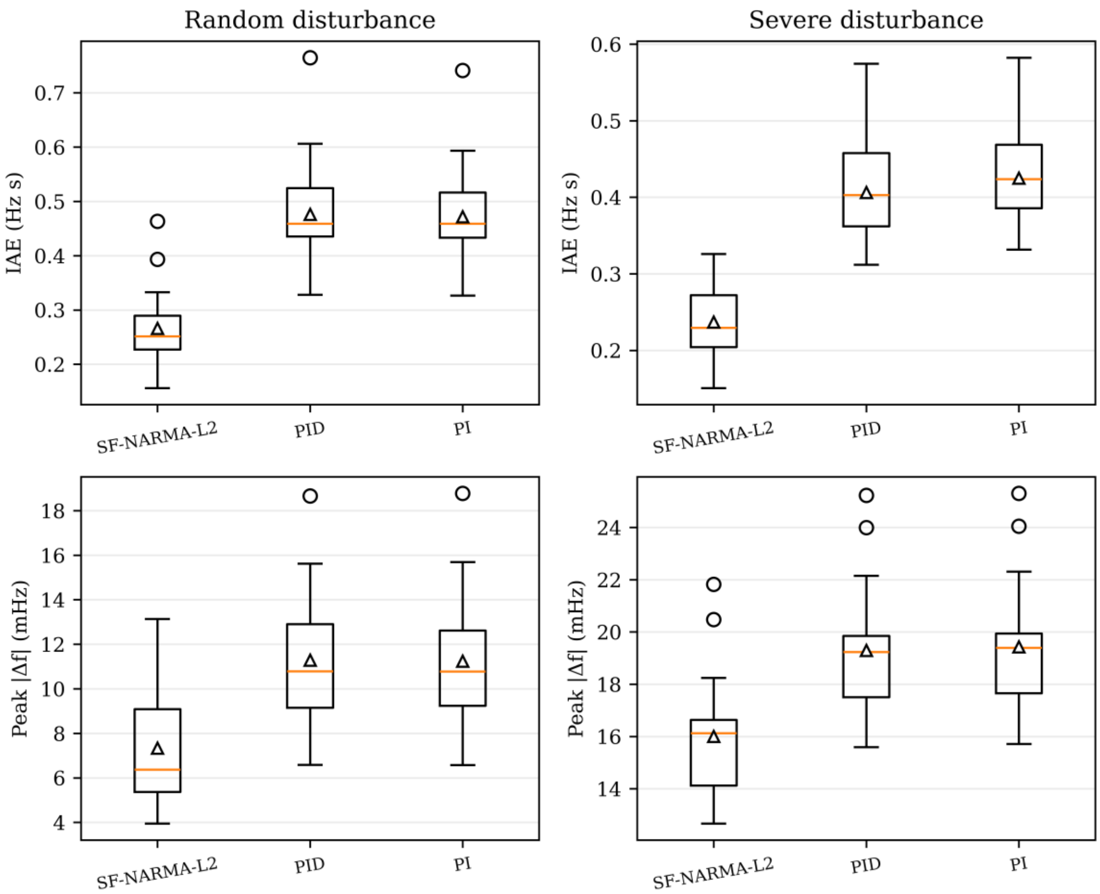

Fig. 9. Twenty-plant Monte Carlo robustness under random and severe solar-load disturbances.

Table 4. Monte Carlo statistics over twenty uncertain plants.

Case	Controller	Peak, mean ± SD (mHz)	RMS, mean ± SD (mHz)	IAE, mean ± SD (Hz·s)	Worst IAE (Hz·s)	Mean RMS u (pu)	Mean TV u (pu)
Random	SF-NARMA-L2	7.332 ± 2.792	2.387 ± 0.657	0.2663 ± 0.0716	0.4631	0.0723	6.106
	PI	11.242 ± 2.830	4.166 ± 0.901	0.4716 ± 0.0984	0.7411	0.0346	0.609
	PID	11.286 ± 2.808	4.205 ± 0.943	0.4762 ± 0.1032	0.7644	0.0379	0.800
Severe	SF-NARMA-L2	16.005 ± 2.361	3.135 ± 0.536	0.2371 ± 0.0535	0.3261	0.0553	1.153
	PI	19.434 ± 2.362	4.614 ± 0.607	0.4252 ± 0.0633	0.5823	0.0347	0.313
	PID	19.298 ± 2.385	4.510 ± 0.598	0.4064 ± 0.0683	0.5745	0.0418	0.398

The Monte Carlo study also reinforces the actuator trade-off. For random forcing, mean command total variation is 6.106 pu for SF-NARMA-L2, compared with 0.800 pu for PID. The result does not invalidate the frequency advantage, but it defines the next design step: the validation objective can be augmented by a plant-specific fatigue or maintenance cost.

H. Lyapunov audit

The locally linearized eigenvalues in Fig. 10 lie strictly inside the unit circle. Table 5 reports positive minimum eigenvalues of P for all controllers. The spectral radii are 0.997295, 0.996442, and 0.996900 for PI, PID, and SF-NARMA-L2, respectively. PID has the smallest local spectral radius, yet it does not provide the best nonlinear disturbance rejection. This is not contradictory. The Lyapunov audit characterizes small unforced perturbations around one equilibrium; it does not encode finite-amplitude PV context, hydraulic inversion, or saturation. The simulation metrics evaluate those effects directly.

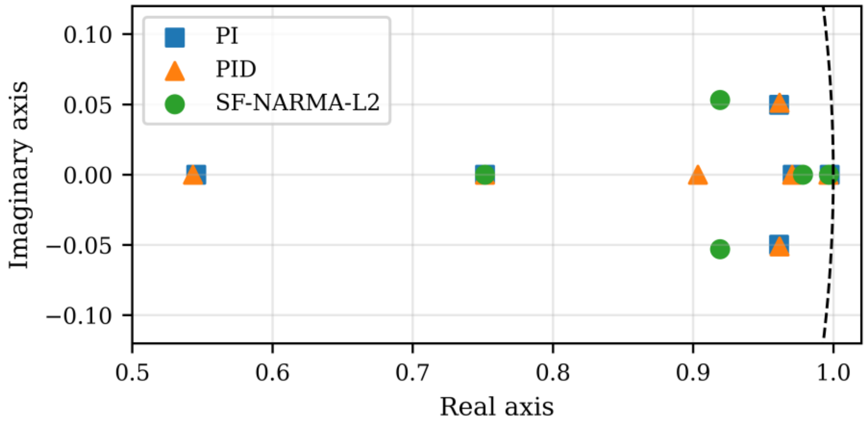

Fig. 10. Eigenvalues of the locally linearized sampled-data closed loops

Table 5. Discrete-time Lyapunov stability audit.

Controller	$\rho(A_{cl})$	$\lambda_{min}(P)$	$\lambda_{max}(P)$
PI	0.997295	1.4180	1397.45
PID	0.996442	1.0000	1505.34
SF-NARMA-L2	0.996900	1.1413	2726.81

VIII. CONCLUSION

A scaling-factor-tuned NARMA-L2 neural controller has been developed for frequency regulation of a hydropower plant subject to distributed PV variability. The benchmark retains the turbine's non-minimum-phase behavior, transient droop, generator-load dynamics, PV lag, and physical gate constraints. The NARMA-L2 model is trained over a ±25% parameter family, and its output scaling factor is selected by a reproducible multi-scenario objective.

The proposed controller achieves the lowest peak, RMS, IAE, and ITAE frequency indices in all four principal tests. Relative to PID, IAE decreases by 39.1-44.3%, while peak deviation decreases by 15.8-23.6%. Twenty-plant Monte Carlo tests preserve the same ranking. The local closed-loop models are Schur stable, and the discrete Lyapunov solutions are positive definite. The method requires greater command variation, particularly under random forcing, although the prescribed command, gate-position, and gate-rate limits remain satisfied.

The evidence therefore supports a qualified conclusion. SF-NARMA-L2 offers stronger disturbance attenuation and parameter robustness when renewable variability is the dominant concern. PI and PID remain simpler and less active. Future work should incorporate fatigue-aware online scaling, measurement delay, PV forecast error, elastic water-hammer dynamics, and hardware-in-the-loop validation.

REFERENCES

[1] W. Guo and J. Yang, "Modeling and dynamic response control for primary frequency regulation of hydro-turbine governing system with surge tank," *Renewable Energy*, vol. 121, pp. 173-187, 2018, doi: 10.1016/j.renene.2018.01.022.

[2] J. Gao, L. Dai, X. Liu, X. Du, D. Luo, and S. Huang, "Variable-speed hydropower generation: System modeling, optimal control, and experimental validation," *IEEE Transactions on Industrial Electronics*, vol. 68, no. 11, pp. 10902-10912, 2021, doi: 10.1109/TIE.2020.3031528.

[3] T. I. Reigstad and K. Uhlen, "Variable speed hydropower conversion and control," *IEEE Transactions on Energy Conversion*, vol. 35, no. 1, pp. 386-393, 2020, doi: 10.1109/TEC.2019.2943233.

[4] N. Kishor, R. P. Saini, and S. P. Singh, "A review on hydropower plant models and control," *Renewable and Sustainable Energy Reviews*, vol. 11, no. 5, pp. 776-796, 2007, doi: 10.1016/j.rser.2005.06.003.

[5] H. Bevrani, *Robust Power System Frequency Control*, 2nd ed. Cham, Switzerland: Springer, 2014, doi: 10.1007/978-3-319-07278-4.

[6] C. K. Shiva, V. Mukherjee, and S. P. Ghoshal, "Automatic generation control of hydropower systems using a novel quasi-oppositional harmony search algorithm," *Electric Power Components and Systems*, vol. 44, pp. 1478-1491, 2016, doi: 10.1080/15325008.2016.1147103.

[7] S. Prasad, S. Purwar, and N. Kishor, "Non-linear sliding mode load frequency control in multi-area power system," *Control Engineering Practice*, vol. 61, pp. 81-92, 2017, doi: 10.1016/j.conengprac.2017.02.001.
[8] M. Ranjan and R. Shankar, "A literature survey on load frequency control considering renewable energy integration in power system: Recent trends and future prospects," *Journal of Energy Storage*, vol. 45, Art. no. 103717, 2022, doi: 10.1016/j.est.2021.103717.
[9] H. H. Alhelou, M. E. H. Golshan, R. Zamani, E. Heydarian-Forushani, and P. Siano, "Challenges and opportunities of load frequency control in conventional, modern and future smart power systems: A comprehensive review," *Energies*, vol. 11, no. 10, Art. no. 2497, 2018, doi: 10.3390/en11102497.
[10] K. Ullah, A. Basit, Z. Ullah, S. Aslam, and H. Herodotou, "Automatic generation control strategies in conventional and modern power systems: A comprehensive overview," *Energies*, vol. 14, no. 9, Art. no. 2376, 2021, doi: 10.3390/en14092376.
[11] H. Ali, G. Magdy, and D. Xu, "A new optimal robust controller for frequency stability of interconnected hybrid microgrids considering non-inertia sources and uncertainties," *International Journal of Electrical Power & Energy Systems*, vol. 128, Art. no. 106651, 2021, doi: 10.1016/j.ijepes.2020.106651.
[12] S. M. Abd-Elazim and E. S. Ali, "Load frequency controller design of a two-area system composing of PV grid and thermal generator via firefly algorithm," *Neural Computing and Applications*, vol. 30, pp. 607-616, 2018, doi: 10.1007/s00521-016-2668-y.
[13] G. Magdy, G. Shabib, A. A. Elbaset, and Y. Mitani, "A novel coordination scheme of virtual inertia control and digital protection for microgrid dynamic security considering high renewable energy penetration," *IET Renewable Power Generation*, vol. 13, no. 3, pp. 462-474, 2019, doi: 10.1049/iet-rpg.2018.5513.
[14] A. Saxena and R. Shankar, "Improved load frequency control considering dynamic demand regulated power system integrating renewable sources and hybrid energy storage system," *Sustainable Energy Technologies and Assessments*, vol. 52, Art. no. 102245, 2022, doi: 10.1016/j.seta.2022.102245.
[15] V. P. Singh, N. Kishor, and P. Samuel, "Improved load frequency control of power system using LMI based PID approach," *Journal of the Franklin Institute*, vol. 354, pp. 6805-6830, 2017, doi: 10.1016/j.jfranklin.2017.08.031.
[16] Y. Arya, "Automatic generation control of two-area electrical power systems via optimal fuzzy classical controller," *Journal of the Franklin Institute*, vol. 355, pp. 2662-2688, 2018, doi: 10.1016/j.jfranklin.2018.02.004.
[17] N. Jalali, H. Razmi, and H. Doagou-Mojarrad, "Optimized fuzzy self-tuning PID controller design based on Tribe-DE optimization and rule-weight adjustment for load frequency control of interconnected multi-area power systems," *Applied Soft Computing*, vol. 93, Art. no. 106424, 2020, doi: 10.1016/j.asoc.2020.106424.
[18] A. M. A. Soliman et al., "PSO tuned interval type-2 fuzzy logic for load frequency control of two-area multi-source interconnected power system," *Scientific Reports*, vol. 13, Art. no. 8724, 2023, doi: 10.1038/s41598-023-35454-4.
[19] V. Çelik, "Effects of fractional-order PI controller on delay margin in single-area delayed load frequency control systems," *Journal of Modern Power Systems and Clean Energy*, vol. 7, pp. 380-389, 2019, doi: 10.1007/s40565-018-0458-5.
[20] J. Guo, "Application of full order sliding mode control based on different areas power system with load frequency control," *ISA Transactions*, vol. 92, pp. 23-34, 2019, doi: 10.1016/j.isatra.2019.01.036.
[21] J. Guo, "Application of a novel adaptive sliding mode control method to the load frequency control," *European Journal of Control*, vol. 57, pp. 172-178, 2021, doi: 10.1016/j.ejcon.2020.03.007.
[22] Z. Yan and Y. Xu, "A multi-agent deep reinforcement learning method for cooperative load frequency control of a multi-area power system," *IEEE Transactions on Power Systems*, vol. 35, no. 6, pp. 4599-4608, 2020, doi: 10.1109/TPWRS.2020.2999890.
[23] Y. Ma, Z. Hu, and Y. Song, "A reinforcement learning based coordinated but differentiated load frequency control method with heterogeneous frequency regulation resources," *IEEE Transactions on Power Systems*, vol. 39, no. 1, pp. 2239-2250, 2024, doi: 10.1109/TPWRS.2023.3262543.
[24] P. Sharma, "NARMA-L2 controller for five-area load frequency control," *Indonesian Journal of Electrical Engineering and Informatics*, vol. 2, no. 4, pp. 170-179, 2014, doi: 10.52549/ijeei.v2i4.123.
[25] D. K. Sambariya and V. Nath, "Application of NARMA L2 controller for load frequency control of multi-area power system," in *Proc. 10th International Conference on Intelligent Systems and Control*, 2016, pp. 1-7, doi: 10.1109/ISCO.2016.7726987.
[26] A. Gundogdu and R. Celikel, "NARMA-L2 controller for stepper motor used in single-link manipulator with low-speed-resonance damping," *Engineering Science and Technology, an International Journal*, vol. 24, no. 2, pp. 360-371, 2021, doi: 10.1016/j.jestch.2020.09.008.
[27] G.-B. Huang, Q.-Y. Zhu, and C.-K. Siew, "Extreme learning machine: Theory and applications," *Neurocomputing*, vol. 70, pp. 489-501, 2006, doi: 10.1016/j.neucom.2005.12.126.
[28] G.-B. Huang, H. Zhou, X. Ding, and R. Zhang, "Extreme learning machine for regression and multiclass classification," *IEEE Transactions on Systems, Man, and Cybernetics, Part B*, vol. 42, no. 2, pp. 513-529, 2012, doi: 10.1109/TSMCB.2011.2168604.
[29] T. Weldcherkos, A. O. Salau, and A. Ashagrie, "Modeling and design of an automatic generation control for hydropower plants using neuro-fuzzy controller," *Energy Reports*, vol. 7, pp. 6626-6637, 2021, doi: 10.1016/j.egyr.2021.09.143.
[30] Y. Arya, P. Dahiya, E. Çelik, G. Sharma, H. Gözde, and I. Nasiruddin, "AGC performance amelioration in multi-area interconnected thermal and thermal-hydro-gas power systems using a novel controller," *Engineering Science and Technology, an International Journal*, vol. 24, no. 2, pp. 384-396, 2021, doi: 10.1016/j.jestch.2020.08.015.
[31] R. K. Sahu, S. Panda, and U. K. Rout, "Automatic generation control of multi-area power systems with diverse energy sources using teaching-learning-based optimization algorithm," *Engineering Science and Technology, an International Journal*, vol. 19, pp. 113-134, 2016, doi: 10.1016/j.jestch.2015.07.011.
[32] V. V. Huynh et al., "Load frequency control for multi-area power plants with integrated wind resources," *Applied Sciences*, vol. 11, no. 7, Art. no. 3051, 2021, doi: 10.3390/app11073051.
[33] V. V. Huynh et al., "Highly robust observer sliding-mode-based frequency control for multi-area power systems with renewable power plants," *Electronics*, vol. 10, no. 3, Art. no. 274, 2021, doi: 10.3390/electronics10030274.
[34] M. K. Sarkar and A. Dev, "Chattering-free robust adaptive integral higher-order sliding mode control for load frequency problems in multi-area power systems," *IET Control Theory & Applications*, vol. 12, pp. 1216-1227, 2018, doi: 10.1049/iet-cta.2017.0735.

[35] W. Shangguan et al., "Control-performance-standards-oriented event-triggered load frequency control for power systems under limited communication bandwidth," *IEEE Transactions on Control Systems Technology*, vol. 30, no. 2, pp. 860-868, 2022, doi: 10.1109/TCST.2021.3070861.
[36] S. Prasad, S. Purwar, and N. Kishor, "Load frequency regulation using observer-based non-linear sliding mode control," *International Journal of Electrical Power & Energy Systems*, vol. 104, pp. 178-193, 2019, doi: 10.1016/j.ijepes.2018.06.035.